Critical phenomena in the general spherically symmetric Einstein-Yang-Mills system

Maciej Maliborski[*]

Faculty of Physics, University of Vienna, Boltzmanngasse 5, A1090 Wien, Austria
and Max Planck Institute for Gravitational Physics (Albert Einstein Institute),
Am Mühlenberg 1, 14476 Potsdam, Germany

Oliver Rinne[†]

Hochschule für Technik und Wirtschaft Berlin, Treskowallee 8, 10318 Berlin, Germany
and Max Planck Institute for Gravitational Physics (Albert Einstein Institute),
Am Mühlenberg 1, 14476 Potsdam, Germany

We study critical behavior in gravitational collapse of a general spherically symmetric Yang-Mills field coupled to the Einstein equations. Unlike the magnetic ansatz used in previous numerical work, the general Yang-Mills connection has two degrees of freedom in spherical symmetry. This fact changes the phenomenology of critical collapse dramatically. The magnetic sector features both type I and type II critical collapse, with universal critical solutions. In contrast, in the general system type I disappears and the critical behavior at the threshold between dispersal and black hole formation is always type II. We obtain values of the mass scaling and echoing exponents close to those observed in the magnetic sector, however we find some indications that the critical solution differs from the purely magnetic discretely self-similar attractor and exact self-similarity and universality might be lost. The additional "type III" critical phenomenon in the magnetic sector, where black holes form on both sides of the threshold but the Yang-Mills potential is in different vacuum states and there is a mass gap, also disappears in the general system. We support our dynamical numerical simulations with calculations in linear perturbation theory; for instance, we compute quasi-normal modes of the unstable attractor (the Bartnik-McKinnon soliton) in type I collapse in the magnetic sector.

I. INTRODUCTION

The Einstein-Yang-Mills (EYM) equations form a particularly rich dynamical system already in spherical symmetry. This is due to the existence of nontrivial static and discretely self-similar solutions, which play the role of unstable attractors.

The general spherically symmetric Yang-Mills (YM) connection has two free potentials w and ω (see Sec. II for details). Most numerical work so far (e.g. [1–6]) has imposed in addition to spherical symmetry the so-called *magnetic ansatz* $\omega = 0$. The term "magnetic" originates from the fact that for a static spacetime, the YM curvature only has a magnetic part and no electric part in this case. This ansatz is self-consistent in the sense that if the initial data satisfy $\omega = 0$ then this remains so at all times. In contrast, if the so-called *sphaleronic sector* is turned on by allowing $\omega \neq 0$ in the initial data, then both w and ω will be nonzero during the evolution. (The term "sphaleron" [7]

appears to refer to similar solutions to the Yang-Mills-Higgs equations; note there is no Higgs field here though.) Hence the magnetic sector forms a subsystem of the most general spherically symmetric EYM equations, which we sometimes also refer to as the extended system.

As far as we know, so far the only numerical evolutions of the extended system have been presented in [8], even though the equations have been worked out before, e.g. in [2]. The paper [8] was mainly concerned with power-law tails. The aim of the present paper is to study critical phenomena in gravitational collapse in the extended system.

In critical collapse one chooses a one-parameter (usually denoted by p) family of initial data such that (at least in the standard definition) a black hole forms in the subsequent evolution for $p > p_*$ and the field disperses to flat spacetime for $p < p_*$. One now asks what happens close to the critical point $p = p_*$. For surveys of critical collapse of various matter models coupled to the Einstein equations, we refer the reader to [9–11].

Let us first review the situation in the magnetic sector of the EYM system. Depending on the family of initial data, two different types of critical behavior occur.

[*]maciej.maliborski@univie.ac.at
[†]oliver.rinne@aei.mpg.de

In type I critical collapse [1], black hole formation for $p > p_*$ turns on at a finite (nonzero) value of the black hole mass, and at the critical threshold the evolution approaches a static solution. This static solution is identified as the first member X_1 of a discrete (countably infinite) family of regular static solutions, the *Bartnik-McKinnon solitons* [12].

In type II critical collapse [1], the black hole mass M vanishes as $p \searrow p_*$; more precisely, $M \sim (p - p_*)^\gamma$ with an exponent γ that is universal, i.e. independent of the particular family of initial data chosen. The critical solution is discretely self-similar (for a definition see Eq. (23) below and [11]). The echoing exponent Δ related to the discrete self-similarity as well as the critical solution itself are universal.

There is a third type of critical collapse, which unlike the other two is specific to the YM field used here as a matter model. This is related to the fact that assuming spherical symmetry and the magnetic ansatz, there are two values of the potential w, namely $w = \pm 1$, that both correspond to vacuum (i.e. vanishing YM curvature and hence energy-momentum tensor). In type III collapse one considers a family of initial data that lead to black hole formation for all values of the parameter p, but such that the final value of the YM potential is $w = 1$ for $p > p_*$, say, and $w = -1$ for $p < p_*$. Even though both outcomes correspond to a vacuum black hole, the dynamical evolutions are different and the black hole mass is discontinuous across the threshold [2,6]. The critical solution is static (as in type I) and is identified with the first member Y_1 of a discrete family of static hairy (i.e. with nonzero YM field) black hole solutions, the *colored black holes* [13,14].

For a static or self-similar solution to appear as a critical solution in a one-parameter bisection search, this solution must have precisely one unstable mode when considering linear perturbations [11]. Linear perturbations of the Bartnik-McKinnon solitons X_n and colored black holes Y_n were studied in [7,15]. In the magnetic sector X_n and Y_n both have n unstable modes. So indeed X_1 and Y_1 have precisely one unstable mode in the magnetic sector. However, in the extended system X_n and Y_n have a total of $2n$ unstable modes. Thus X_1 and Y_1 now have two unstable modes, and hence they cannot be codimension-one unstable attractors in the extended system. This indicates that the phenomenology of critical collapse is likely to be very different. It is important to note here that subject to suitable falloff conditions, there are no static solutions with nonzero electric part of the YM curvature except for the Reissner-Nordström solution [16,17]. Hence no nontrivial potential static attractors are added when moving from the magnetic to the general ansatz.

One of our main results is that there is no type I critical collapse in the extended system, instead the critical behavior at the threshold between dispersal and black hole formation is always type II. We compare the critical solution and scaling exponents with those in the magnetic sector. For small sphaleronic perturbations the Bartnik-McKinnon soliton X_1 can be observed as an intermediate attractor before the self-similar type II critical solution is approached. We study in detail how the type II mass scaling sets on when perturbing off data that in the magnetic sector would be type I-critical.

We also refine some results in the magnetic sector, namely we find wiggles on top of the power-law scaling of the curvature in subcritical evolutions, which allow for an independent estimate of the type II echoing exponent. In type I collapse in the magnetic sector, we show how X_1 is approached via a quasinormal mode (QNM) and a tail, and we compare with a calculation of the QNM frequency in linear perturbation theory.

Concerning type III collapse, once a small sphaleronic perturbation in ω is added, the discontinuous transitions in the YM potential w and the black hole mass M across the critical threshold are replaced by continuous ones. Thus there is no critical behavior any longer. In the magnetic sector we find tentative evidence of a QNM ringdown to the colored black hole critical solution.

Our numerical results were obtained with two independent codes using different coordinates. The type I and type II simulations employ standard polar-areal (Schwarzschild-like) coordinates. For type III collapse we use hyperboloidal slices of constant mean curvature, which are conformally compactified towards future null infinity. The details of and motivations for these different coordinate choices are explained in Sec. II.

This paper is organized as follows. In Sec. II we describe our ansatz for YM connection in spherical symmetry and our choices of spacetime coordinates. Our numerical results on type I and type II critical collapse are presented in Sec. III, and on type III collapse in Sec. IV. We conclude in Sec. V. Further details are deferred to the appendices: the equations solved by our two codes are given in Appendix A, linear perturbations of the static solutions are analyzed in Appendix B, and a brief summary of our numerical methods can be found in Appendix C.

II. SETUP AND COORDINATE CHOICES

The most general spherically symmetric YM connection with gauge group SU(2) can be written in the following form after exploiting the residual SU(2) gauge freedom [18,19]:

$$\mathcal{A} = u\tau_3 dt + (w\tau_1 + \omega\tau_2)d\theta$$
$$+ (\cot\theta\tau_3 + w\tau_2 - \omega\tau_1)\sin\theta d\phi, \qquad (1)$$

where u, w and ω are functions of t and r only and τ_i form a standard basis of SU(2), $[\tau_i, \tau_j] = \varepsilon_{ijk}\tau_k$, where ε_{ijk} is totally antisymmetric with $\varepsilon_{123} = 1$.

An alternative parametrization of the YM connection, used in [8], is

$$\mathcal{A}^{i(a)} = \varepsilon^{aij}x^j F + (x^a x^i - r^2 \delta^{ai})H,$$

$$\mathcal{A}_0^{(a)} = Gx^a, \qquad (2)$$

where (a) denotes the SU(2) gauge group index, all indices run over 1,2,3 and repeated indices are summed over. The field equations that these two parametrizations give rise to are equivalent; the correspondence between the variables is[1]

$$F = \frac{1+w}{r^2}, \qquad H = -\frac{\omega}{r^3}, \qquad G = \frac{u}{r}. \qquad (3)$$

The magnetic ansatz consists in setting $\omega = u = 0$ (or equivalently $H = G = 0$). It leads to a self-consistent set of field equations. It should be stressed that the additional YM potential ω (or equivalently H) in the general ansatz (1) *cannot* be transformed away by an SU(2) gauge transformation; it forms a second physical degree of freedom, the sphaleronic sector. The function u (or equivalently G) on the other hand can be thought to be determined by w and ω via the YM constraint equation (cf. Appendix A).

We have implemented two different choices of spacetime coordinates. For the simulations of type I and type II critical collapse presented below, we use polar-areal coordinates, in which the line element takes the form

$$ds^2 = -Ae^{-2\delta}dt^2 + \frac{dr^2}{A} + r^2 d\sigma^2, \qquad (4)$$

where $d\sigma^2$ denotes the standard round metric on the two-sphere.

For the simulations of type III critical collapse, we use constant-mean-curvature (CMC) slices and isotropic spatial coordinates,

$$ds^2 = \Omega^{-2}[-\tilde{N}^2 dt^2 + (dr + rX dt)^2 + r^2 d\sigma^2]. \qquad (5)$$

The reason is that black holes form on both sides of the critical threshold in type III collapse, and polar slices cannot penetrate black hole horizons, whereas CMC slices can. Furthermore, CMC slices extend to future null infinity, which provides a natural boundary of the computational domain where no boundary conditions need to be imposed as all the characteristics leave the domain. Hence very long evolutions unspoilt by any effects of an artificial timelike outer boundary are possible.

The EYM field equations in the two different formulations are given in Appendix A.

---

[1]The gauge transformation $\mathcal{A} \to U\mathcal{A}U^{-1} + UdU^{-1}$ with $U = e^{\theta\tau_1}e^{(\pi/2-\varphi)\tau_3}$ transforms (2) into (1). We note that changing the sign of w and ω simultaneously leaves the field equations invariant.

III. TYPE I AND TYPE II COLLAPSE

In this section we present our numerical results on type I and type II critical behavior both in the magnetic sector and the sphaleronic sector. These simulations were carried out using the code based on polar-areal coordinates.

A. Initial data

In our studies of critical phenomena we experimented with different choices of initial data but for clarity we present our results for three particular families:

(i) a localized Gaussian perturbation

$$w(0,r) = 1 + a_1 \exp\left[-\left(\frac{r-x_1}{s_1}\right)^{2q_1}\right], \qquad (6)$$

$$\omega(0,r) = a_2\left(\frac{r}{x_2}\right)^3 \exp\left[-\left(\frac{r-x_2}{s_2}\right)^{2q_2}\right], \qquad (7)$$

$$\Pi(0,r) = \partial_r w(0,r), \qquad (8)$$

$$P(0,r) = 0, \qquad (9)$$

(ii) kinklike data

$$w(0,r) = 1 - a_1 \tanh\left(\frac{r}{s_1}\right)^{q_1}, \qquad (10)$$

$$\omega(0,r) = -a_2 \tanh\left(\frac{r}{s_2}\right)^{q_2}, \qquad (11)$$

$$\Pi(0,r) = \frac{r}{s_1}\partial_r w(0,r), \qquad (12)$$

$$P(0,r) = \frac{r}{s_2}\partial_r \omega(0,r), \qquad (13)$$

(iii) and purely magnetic kinklike data

$$w(0,r) = 1 + a_1\left[-2\tanh\left(\frac{r}{s_1}\right)^{q_1} + 2\tanh\left(\frac{r}{s_2}\right)^{q_2}\right], \qquad (14)$$

$$\omega(0,r) = 0, \qquad (15)$$

$$\Pi(0,r) = a_2\left[\frac{r}{s_1}\partial_r\left(-2\tanh\left(\frac{r}{s_1}\right)^{q_1}\right)\right. \qquad (16)$$

$$\left. + \frac{r}{s_2}\partial_r\left(2\tanh\left(\frac{r}{s_2}\right)^{q_2}\right)\right], \qquad (17)$$

$$P(0,r) = 0. \qquad (18)$$

Here the auxiliary variables Π and P are essentially time derivatives of w and ω [cf. Eqs. (A1), (A2)] and are set to

make w and ω either approximately ingoing or stationary initially. We note that this parametrization of the fields has been chosen to be consistent with the following regularity conditions at the origin, which follow from a Taylor expansion of the field equations:

$$w = 1 + \mathcal{O}(r^2), \qquad \omega = \mathcal{O}(r^3) \qquad (19)$$

[from which we also get analogous behavior of Π and P, see (A1)–(A2)]. Asymptotic flatness requires

$$w^2 + \omega^2 \to 1 \quad \text{as } r \to \infty, \qquad (20)$$

which has to be satisfied by the initial data; in particular for kink-like data (ii) this condition introduces the constraint $a_2^2 = a_1(2 - a_1)$. The choice of parameters will be discussed below depending on the situation considered.

B. Magnetic sector

We begin by restricting ourselves to the magnetic sector for family (i), i.e. $a_2 = 0$ in (7). Here we observe both type I and type II critical behavior as previously analyzed in [1].

1. Type II collapse

First we investigate type II critical collapse. For this we vary $p := a_1$ in (6) and fix the remaining parameters to $s_1 = 1/4$, $x_1 = 3$ and $q_1 = 1$. The value of the critical amplitude is found to be $p_* \approx 0.147\,83$. We observe a universal scaling of the mass of the apparent horizon in supercritical evolutions

$$M_{\text{AH}} \sim (p - p_*)^\gamma \qquad (21)$$

with $\gamma = 0.20018 \pm 0.00017$, and also a polynomial scaling of $\mathcal{R}^2 := R_{\mu\nu} R^{\mu\nu}|_{r=0}$ in subcritical evolutions

$$\mathcal{R}^2 \sim (p - p_*)^{-4\gamma} \qquad (22)$$

with the exponent $-4\gamma = -0.7886 \pm 0.0029$, i.e. $\gamma = 0.19714 \pm 0.00074$. These values for γ are consistent with the value $\gamma \approx 0.20$ reported in [1] and with the result $\gamma = 0.1964 \pm 0.0007$ obtained by directly computing the critical solution and its perturbations [20]. The discrepancy of the super- and subcritical scaling exponents γ obtained from time evolutions of near critical data results mainly from the inaccurate estimate of the apparent horizon in the supercritical case. The scaling exponent we find in subcritical evolutions is much more accurate and is closer to the value of [20].

In a graph of $\log \mathcal{R}^2$ vs $\log |p_* - p|$ we see periodic wiggles on top of the straight line, which are shown in Fig. 1. From the fit to the numerical data we determine the period of oscillation to be $\tau_\mathcal{R} \approx 0.815$, which is roughly comparable to the theoretical prediction in [21],
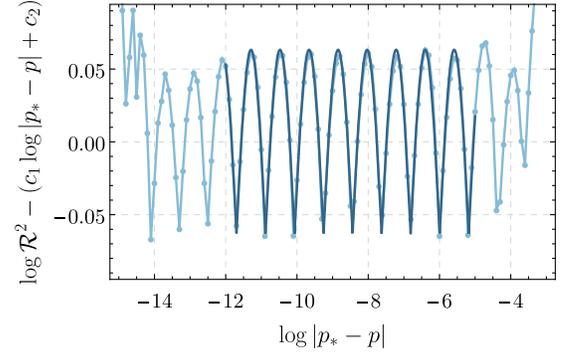
FIG. 1. An analysis of subcritical data in type II critical behavior. Data (points) of $\log \mathcal{R}^2$ are compared with a five-parameter fit $c_1 q + c_2 + c_3 |\cos(c_4 q + c_5) - 1/2|$, where $q := \log |p_* - p|$, after subtraction of the linear part. Our choice of periodic function for q is rather *ad hoc* and is justified by its relatively good agreement with the numerical data.

$\Delta/(4\gamma) \approx 0.939$ (with the values of Δ and γ taken from [20]), where Δ is the echoing exponent discussed in the following.

The solution in the near-critical regime shows the approximate scaling symmetry[2]

$$Z(\tau - \Delta_\tau, \rho - \Delta_\rho) = Z(\tau, \rho) \qquad (23)$$

for a scale-free variable Z in terms of logarithmic coordinates

$$\rho = \ln r, \qquad \tau = \ln(T_0^* - T_0), \qquad (24)$$

where T_0 denotes proper time at the origin[3] and T_0^* is the accumulation time of the type II critical solution. This is depicted for the scale-free variable $w' := \partial_r w$ in Fig. 2. The spatial echoing exponent Δ_ρ determined by rescaling the spatial profiles at times at which the profiles overlap is found to be $\Delta_\rho \approx 0.736 \pm 0.001$. From a discrete set of such matching times we estimate the temporal period $\Delta_\tau \approx 0.7364 \pm 0.0007$ (we also get an estimate for the collapse time T_0^*, however this depends on the initial data). These results support the claim that $\Delta_\rho = \Delta_\tau =: \Delta$ and are consistent with the value $\Delta \approx 0.74$ reported in [1] as well as the refined value $\Delta = 0.73784 \pm 0.00002$ in [20].

Universality of the critical solution is demonstrated in Fig. 3, where we compare spatio-temporal profiles of solutions obtained through bisection search starting from the different initial conditions (i) and (iii). We do this by

---

[2]That this is only an approximate symmetry follows from the existence of a scale in the EYM system set by the YM coupling constant. However close to the critical point this scale becomes irrelevant and thus (23) holds [20].

[3]T_0 coincides with the coordinate time t used in our code (see Appendix A).
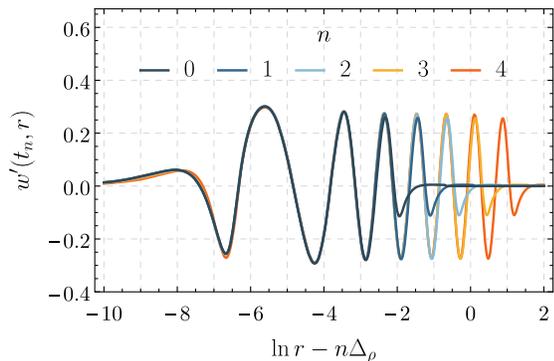
FIG. 2. An illustration of the discrete self-similarity of the critical solution in type II critical collapse within the magnetic ansatz. This plot should be compared with Fig. 3 of [1].

plotting a suitably rescaled invariant I_1 defined in (A13) with respect to the coordinates (24).

2. Type I collapse

Next we turn to type I critical behavior, still in the magnetic sector. We consider initial data family (i) and vary $p := a_1$ in (6), fixing the remaining parameters to $s_1 = 4$, $x_1 = 10$ and $q_1 = 2$. The critical amplitude at the threshold between dispersal and black hole formation is $p_* \approx -1.352\,32$. As discovered in [1], the $n = 1$ Bartnik-McKinnon soliton X_1, which has one unstable mode in the magnetic sector, plays the role of the critical solution. Our numerical simulations reproduce this behavior.

In addition, we investigate more closely how the dynamical solutions approach the intermediate attractor. In Appendix B we carry out a linear perturbation analysis about X_1, which confirms the unstable mode with exponent $\lambda \approx 2.562\,79$. In addition, we have found quasinormal

modes (QNM), the least damped of which has $\lambda = -1.402\,33 \pm 3.603\,51i$. Figure 4 shows the different phases of the evolution: approach to the unstable attractor X_1 via QNM and polynomial tail, and departure along the unstable mode. The fitted values of the QNM and unstable mode agree well with the prediction. The tail does not appear for a sufficiently long time to allow for a conclusive determination of the decay exponent p; our numerical fit yields $p = -4.801$. (For comparison, the tail on a Schwarzschild or Minkowski background has exponent $p = -4$ [22].)

As is characteristic of type I critical behavior, we observe a saturation of the black hole mass in supercritical evolutions as a function of the parameter distance from the critical solution. The mass gap converges to the approximate value 0.5802, which is close to but slightly less than the mass of the X_1 solution [12], $M_{X_1} = 0.585942$. As the apparent horizon forms, a fraction of the energy associated with X_1 stays outside of the trapped region, and this excess of mass escapes to infinity (however with our numerical code we are unable to follow this part of the evolution).

Moreover, on a plot of M vs $\log |p_* - p|$ we observe a damped oscillation, see Fig. 5, whose origin may be explained as follows. As discussed above, the linear analysis of X_1 predicts the existence of both stable and unstable modes. Thus close to the critical point $p \approx p_*$ the dynamical solution $w(t, r)$ consist of the attractor $w_s(r)$ and its linear perturbation of the form

$$w(t, r) = w_s(r) + \phi_{UN}(r)|p_* - p|e^{\lambda t} + \phi_{QNM}(r)\sin(\Omega t)e^{-\Gamma t} + \cdots, \quad (25)$$

where $\lambda > 0$ is the exponent of the unstable mode, the third term represents the dominant QNM with $\Gamma > 0$, and the
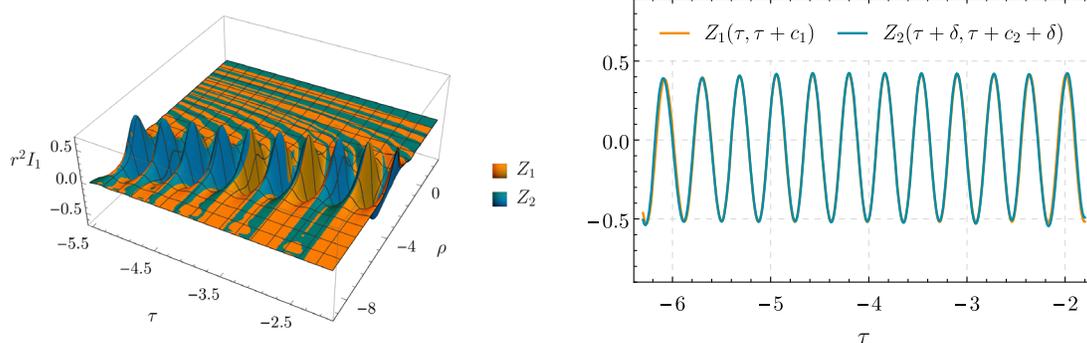
FIG. 3. Universality of the type II critical solution in the magnetic ansatz. We plot the spatio-temporal profile of the scale-invariant quantity $Z := r^2 I_1$, where the invariant I_1 is defined in (A13) (note that the period is $\Delta/2$ because this quantity is quadratic in dynamical variables). Two critical solutions were generated by a bisection search starting from the different initial conditions (i) and (iii) (for the latter we take $a_1 = a_2 = 1$, $s_1 = 2$, $s_2 = p$, $q_1 = q_2 = 2$). Having two solutions Z_1, Z_2 expressed in terms of the coordinates (τ, ρ) defined in (24), we are allowed to perform any translation of one of them such that both coincide. [In practice we minimize the difference $\|Z_1(\tau, \rho) - Z_2(\tau + \delta_1, \rho + \delta_2)\|$ in some suitable norm over the shift parameters (δ_1, δ_2).] If the phenomenon is universal then both solutions should agree asymptotically as $(\tau, \rho) \to (-\infty, -\infty)$, which is demonstrated here. The right plot shows the aligned profiles along the particular line $\tau - \rho = $ const passing through the local extrema closest to the origin.
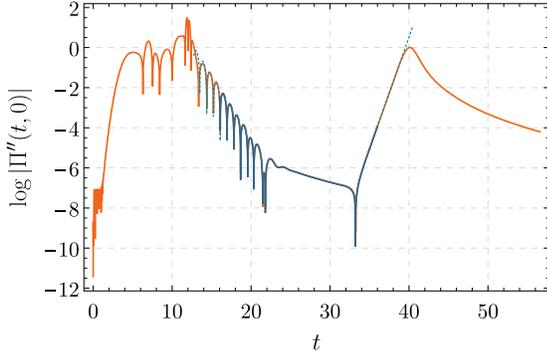
FIG. 4. Subcritical evolution in type I critical collapse (orange) and the best-fit (blue; solid in the fitting range) of a linear combination of QNM, polynomial tail, and unstable mode of X_1. The fitting formula is $c_1 \sin(\Omega(t-15) + c_2) \exp(-\Gamma(t-15)) + c_3 t^p \exp(c_4/t + c_5/t^2) + c_6 \exp(\lambda(t-34))$. The relevant parameters for this plot are $\Omega = 3.639$, $\Gamma = 1.426$, $p = -4.801$, and $\lambda = 2.563$.

dots represent faster decaying modes and (possibly) the power law tail. Performing bisection in one parameter p, we effectively cancel the unstable mode only but the magnitude of the QNM is not under control. Therefore what contributes to the apparent horizon mass is the static solution X_1 itself and its least damped QNM. Because the latter oscillates (in time), its magnitude will depend on the time spent close to X_1, which in turn depends on λ and
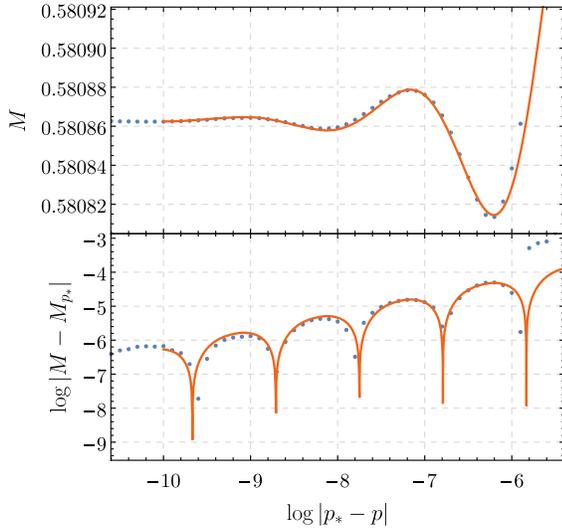
FIG. 5. Mass of the apparent horizon in type I critical collapse as a function of the logarithm of the critical separation. For finite separation the mass oscillates around the asymptotic value M_{p_*}, which is slightly smaller than the mass of the critical solution X_1. This "damped oscillation" is suggested to be an imprint of the least damped QNM of X_1 (see the discussion in the text). The data points are plotted together with the fit $M_{p_*} + c_1 \cos(c_2 \log|p_* - p| + c_3) \exp(c_4 \log|p_* - p|)$, where M_{p_*} and the c_i are fitting parameters.

the distance $|p_* - p|$ from the critical point. A simple calculation shows that one should expect M to oscillate (with respect to $|p_* - p|$) with frequency Ω/λ and damping Γ/λ. However, from the data we get numbers close to $2\Omega/\lambda$ and $2\Gamma/\lambda$ for the frequency and damping respectively. This suggests that the observed phenomenon is not a linear effect.

C. Sphaleronic sector

Next we switch on the sphaleronic sector in the general ansatz (1) for the YM connection. For generic initial data with $\omega \neq 0$ we observe type II critical behavior only. This is not surprising because as explained in Sec. I, the type I critical solution in the magnetic sector, X_1, has an additional unstable mode in the sphaleronic sector [7].

Figure 6 shows the sub- and supercritical scaling of the black hole mass and Riemann curvature invariant for different initial data from family (ii). The scaling exponents, shown in Table I, are close to the values in the magnetic sector (see Sec. III B 1) but deviate well beyond
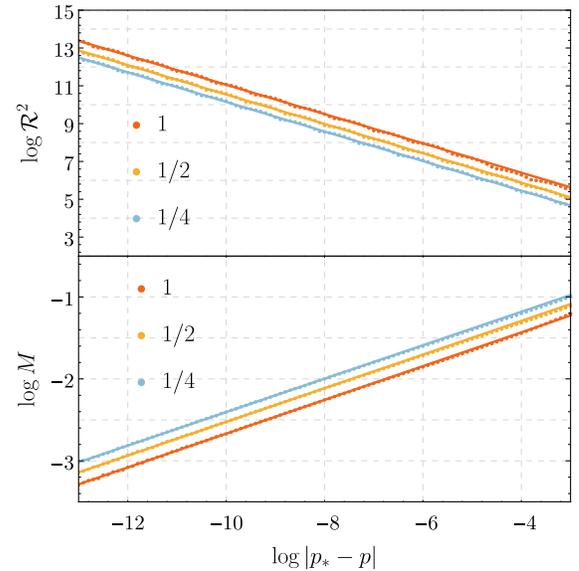
FIG. 6. Supercritical (top) and subcritical (bottom) scaling characterizing type II critical collapse observed within the extended ansatz. The data are plotted with points together with best fits (lines). To produce the plot we used the family of initial data (ii) with bisection parameter $p := s_2$, different values for $a_1 = 1, 1/2, 1/4$ (color-coded in the plot), and $a_2 = \sqrt{a_1(2 - a_1)}$, $s_1 = 3$, $q_1 = 2$, $q_2 = 3$. In each case we find an exponent γ close to the value in the magnetic sector both from super- and subcritical evolutions, see Table I. The plot of $\log \mathcal{R}^2$ vs $\log|p_* - p|$ shows regular oscillations with period very close to the value found in the magnetic sector and consistent with the theoretical prediction (Sec. III B). Similar oscillations, though expected, are less noticeable and less regular on the lower plot due to insufficient resolution. (Precise determination of the location of the apparent horizon requires high resolution at a finite position.) Note the decimal logarithm is used on both plots.

TABLE I. Super- and subcritical scaling exponents γ, see (21)–(22), within the general ansatz for the family of initial data (ii) with parameters as for the data shown in Fig. 6. (The case $a_1 = 0$ would correspond to the magnetic solution, since then also $a_2 = \sqrt{a_1(2 - a_1)} = 0$.)

a_1	γ supercritical	γ subcritical
1	0.20612 ± 0.00037	0.19368 ± 0.00088
1/2	0.20545 ± 0.00031	0.19431 ± 0.00098
1/4	0.20422 ± 0.00028	0.19558 ± 0.00092

the fitting error when the sphaleronic amplitude is increased.

A close examination of the spatial profiles of the critical solution shows that the quantities w' and ω' are almost, but not exactly, scale invariant (Fig. 7). In order to avoid potential gauge effects, we consider the manifestly gauge invariant quantities I_1 (the Lagrangian) and I_2 defined in (A14) and (A15). Figure 7 indicates that while the profiles of I_1 can be made to overlap, those of I_2 at the corresponding times do not. Thus our solution is not exactly self-similar. In any case, from I_1 we extract an echoing exponent $\Delta = 0.7445 \pm 0.0073$ consistent with the value in the magnetic sector.

In Fig. 8 we compare the invariants of the magnetic critical solution with those of the sphaleronic one. There is no exact agreement for the first invariant I_1. Moreover, while the second invariant I_2 is identically zero in the magnetic sector, it is comparable in amplitude to I_1 in the sphaleronic sector. This indicates that the two critical solutions might not be the same. Figure 8 also indicates that there is no perfect universality: I_1 for the critical solutions from two different initial data in the extended system shows reasonably good agreement but I_2 does not.

Our preliminary conclusion is that there are indications that the type II critical solutions in the magnetic sector and in the sphaleronic sector might not be identical, that the sphaleronic critical solution might not be exactly discretely self-similar, and that exact universality might be lost. We did investigate whether these findings might be the caused by numerical errors but could not see any signs of significantly worse convergence of the numerical solution in the sphaleronic sector as compared with the magnetic sector.

We shall leave this question aside for the time being and look more closely at how the type I critical behavior seen in the magnetic sector is transformed into type II behavior when the sphaleronic perturbation is turned on. This is demonstrated in Fig. 9, where we consider the family of initial data (i). We take the same set of parameters as used to produce Fig. 4, but in addition we include a small sphaleronic amplitude a_2, while the bisection parameter is still $p := a_1$. The smaller the sphaleronic perturbation, the closer one needs to tune to the critical point in order to
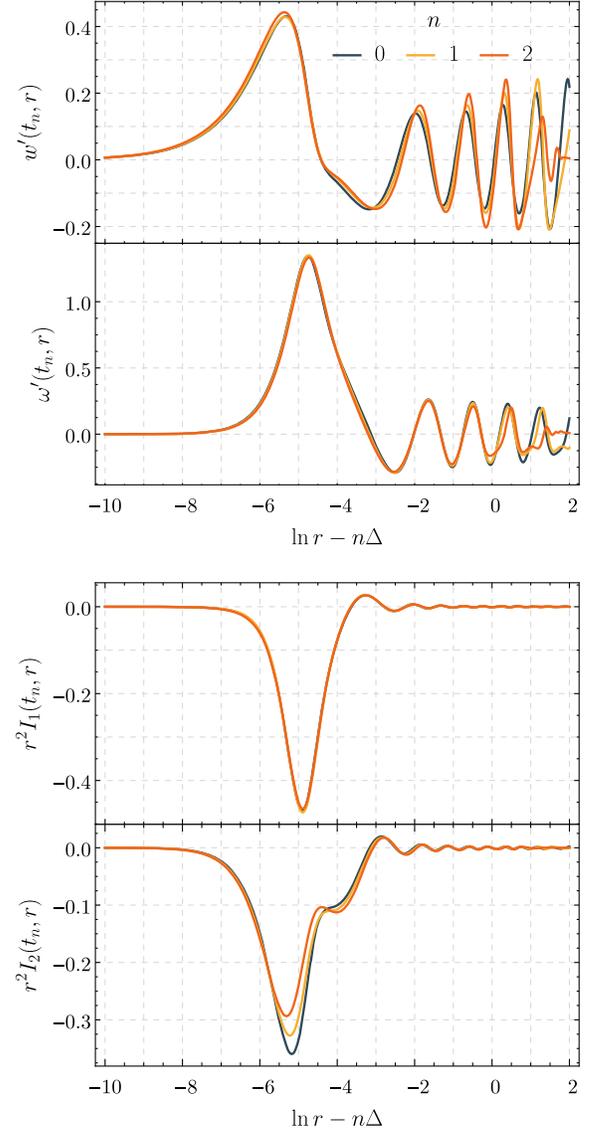
FIG. 7. In the extended system neither w' nor ω' appear to be exactly scale invariant (compare Fig. 2). However, the rescaled invariant $r^2 I_1$ (A13)–(A14) does appear to be discretely self-similar; all presented functions are plotted at times selected to make the shifted profiles of $r^2 I_1$ overlap. We find $\Delta = 0.7445 \pm 0.0073$ for a solution constructed from the initial data (ii) with $a_1 = a_2 = 1$, $s_1 = 2$, $s_2 = p$, $q_1 = 2$, $q_2 = 3$. Observe however that the corresponding profiles of the rescaled second invariant $r^2 I_2$ do *not* overlap.

see the polynomial scaling of the mass and curvature invariant characteristic of type II behavior.

Even though X_1 is not a critical solution in the extended ansatz, it nevertheless plays the role of an intermediate attractor for data close to type I critical data in the magnetic ansatz with a small sphaleronic perturbation. This is illustrated in Fig. 10, where w decays to X_1 by the dominant QNM before it departs along the unstable mode, whereas ω only shows an unstable mode. The fitted exponents agree
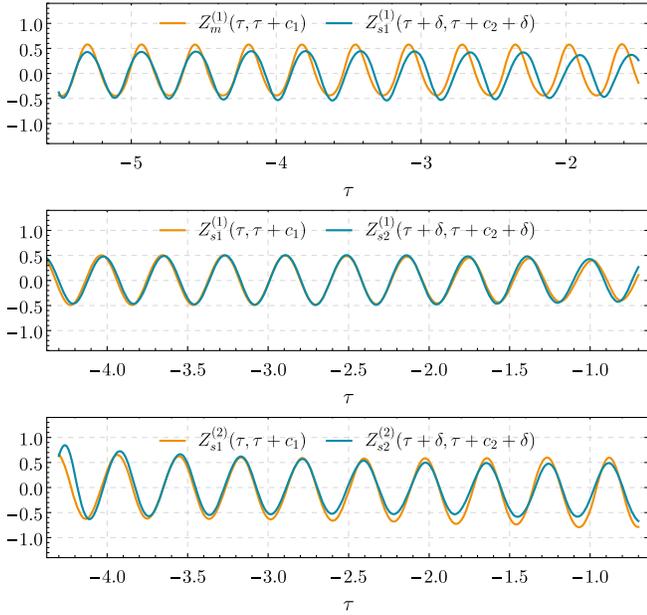
FIG. 8. Comparison of type II critical solutions. We plot the rescaled invariants $Z^{(1)} := r^2 I_1$ and $Z^{(1)} := r^2 I_2$. In the upper plot we present the first invariant, where Z_m refers to the magnetic critical solution obtained in Sec. III B, i.e. we take initial data (i) with $p := a_1$ and $s_1 = 1/4$, $x_1 = 3$, $q_1 = 1$, whereas Z_{s1} was obtained from sphaleronic initial data (ii) with $p := s_2$ and $a_1 = a_2 = 1$, $s_1 = 1$, $q_1 = 2$, $q_2 = 3$. Note that $Z_m^{(2)} \equiv 0$. The middle and bottom plots show two sphaleronic solutions with different initial conditions: family (ii) with $p = s_2$, $a_1 = a_2 = 1$, $q_1 = 2$, $q_2 = 3$ for both solutions, but $s_1 = 2$ for Z_{s1} and $s_1 = 1$ for Z_{s2}. As in Fig. 3 we show the aligned profiles along the line $\tau - \rho = \text{const}$ passing through the local extrema closest to the origin.

well with the predictions from linear perturbation theory (Appendix B), given in brackets: $\lambda \approx -1.419\,95 \pm 3.602\,67i\,(-1.402\,33 \pm 3.603\,51i)$ for the QNM, $\lambda \approx 2.573\,55(2.562\,80)$ for the unstable mode in w and $\lambda \approx 2.782\,96(2.783\,10)$ for the unstable mode in ω.

IV. TYPE III COLLAPSE

In this section we present our numerical results on type III critical behavior. These simulations were carried out using the code based on CMC-isotropic coordinates; the value of the mean extrinsic curvature of the slices is taken to be $K = 1/2$.

A. Initial data

We use the same family of initial data as in [6] consisting of a "kink" and a "bump" in w, and a "bump" in ω:

$$w(0, r) = -\tanh\left(\frac{r - r_k}{\sigma_k}\right) - A_b \exp\left(-\frac{(r - r_b)^2}{2\sigma_b^2}\right), \quad (26)$$
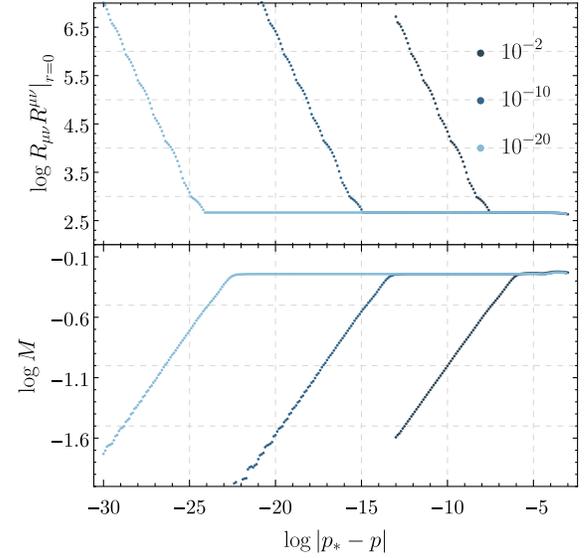
FIG. 9. For initial data (i) the type II critical behavior sets off at a finite distance from the critical point. The onset of the polynomial scaling depends on the strength of the sphaleronic perturbation. The legend shows the amplitude a_2 of ω in initial data class (i). The bisection parameter is $p := a_1$ and the other parameters are fixed to $s_2 = 1/4$, $x_2 = 1$ and $q_2 = 1$.
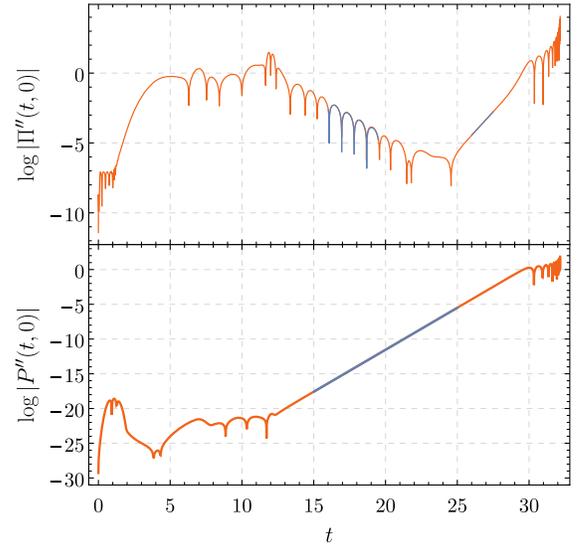
FIG. 10. The Bartnik-McKinnon soliton X_1 as an intermediate attractor of a near-critical evolution in the extended ansatz. Here the sphaleronic perturbation ω in the initial data was held fixed at $a_2 = 10^{-20}$ and the amplitude $p := a_1$ of the initial data for w was tuned to criticality (initial data class (ii), the same as used for Fig. 9). Since this procedure controls only one of the two unstable modes of X_1, this static solution only appears as an intermediate attractor. Ultimately the evolution drifts away from X_1 and echoes of the discretely self-similar type II solution become visible. Compare with Fig. 4.

$$\omega(0,r) = \tilde{A}_b \exp\left(-\frac{(r-\tilde{r}_b)^2}{2\tilde{\sigma}_b^2}\right), \qquad (27)$$

$$\dot{w}(0,r) = \dot{\omega}(0,r) = 0. \qquad (28)$$

B. Magnetic sector

We begin by restricting ourselves to the magnetic sector, i.e. we set $\tilde{A}_b = 0$ in (27). We fix $r_k = 0.4$, $r_b = 0.7$ and $\sigma_b = \sigma_k = 0.05$ in (26) and vary A_b. The critical amplitude is found to be $A_b^* = 1.253\,917\,481\,104\,730\,1$.

The results of our critical search confirm what was dubbed type III critical collapse in [2]. The final states of the evolutions are Schwarzschild black holes with either $w = 1$ or $w = -1$ (dashed line in Fig. 11), both of which correspond to vacuum. At the threshold between the two outcomes, the $n = 1$ colored black hole [13,14], Y_1, is approached as a codimension-one unstable attractor. This solution has one continuous parameter, the horizon (areal) radius, which has the value 2.11 in our case. The masses of the final Schwarzschild black holes as the threshold is approached from either side are different (Fig. 12): in our case $M = 1.235$ for $w = 1$ and $M = 1.090$ for $w = -1$. The dependence of the mass gap on the horizon radius of Y_1 was studied in detail in [6].

Figure 13 shows the different phases of a near-critical evolution: decay Y_1 via QNM, departure along the unstable mode of Y_1, and ringdown to the final Schwarzschild solution via QNM and tail. Unlike for X_1 (Sec. III B), for Y_1 the period of oscillation of the QNM is large compared to the timescale of the unstable mode so that we only see one or two oscillations; this makes a fit difficult. The fitted value of the unstable mode of Y_1, $\lambda = 0.1007$, agrees well with the value $\lambda = 0.1020$ computed from linear perturbation theory in [6]. For the final ringdown to Schwarzschild spacetime, the fitted value of the QNM frequency $\lambda = -0.0835 \pm 0.2222i$ matches the prediction $\lambda = -0.0848 \pm 0.2278i$ from linear perturbation theory ([5], note the QNM frequency scales with M^{-1}, here $M = 1.090$). The tail

FIG. 12. Mass M of the final Schwarzschild black hole as a function of A_b in the magnetic sector ($\tilde{A}_b = 0$, dashed line) and with a sphaleronic perturbation ($\tilde{A}_b = 10^{-2}$, solid line).

could not be resolved properly here due to a lower resolution used in the time-consuming critical bisection search; however for a higher resolution using the same code, the expected [22] exponent $p = -4$ was found in [6], and we will observe the same exponent below in the sphaleronic evolutions.

C. Sphaleronic sector

Next, we add a small perturbation in ω to the initial data: we choose $\tilde{A}_b = 10^{-2}$, $\tilde{r}_b = 0.7$ and $\tilde{\sigma}_b = 0.05$. The discontinuous transition in w as we vary A_b is now replaced by a continuous one, and the final ω also varies continuously (solid lines in Fig. 11). The mass gap also disappears (solid line in Fig. 12).

These findings are not surprising because the dichotomy between the vacua $w = \pm 1$ in the magnetic sector is replaced by a continuum of vacua
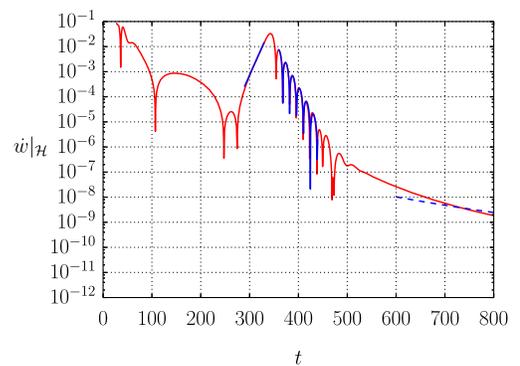
FIG. 13. Time derivative of w at the horizon (after it forms) as a function of time for $\tilde{A}_b = 0$ (magnetic sector) and A_b tuned to criticality (with final value $w = -1$ in this evolution). The solid blue curves are the fits to the unstable mode of Y_1 and the QNM of the final Schwarzschild black hole. The dashed blue curve indicates the expected decay exponent ($p = -4$) of the tail, which is not attained here due to a lower resolution used in the critical bisection search.

FIG. 11. Final values of w (red) and ω (blue) as functions of A_b in the magnetic sector ($\tilde{A}_b = 0$, dashed lines) and with a sphaleronic perturbation ($\tilde{A}_b = 10^{-2}$, solid lines).
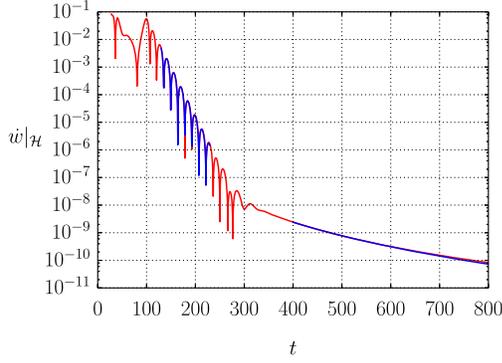
FIG. 14.   Time derivative of w at the horizon (after it forms) as a function of time for $\tilde{A}_b = 10^{-2}$ and the same value for A_b as in the magnetic sector evolution (Fig. 13). The blue curves indicate the fits to the QNM and tail.

$$w^2 + \omega^2 = 1 \qquad (29)$$

in the general system. Hence it is impossible to perform a critical search between two different outcomes. Moreover, as pointed out in Sec. I, Y_1 has an additional unstable mode in the sphaleronic sector [15], hence it cannot appear as a critical solution in the extended system.

Figures 14 and 15 show the dynamical evolution for the value of A_b that corresponded to the critical threshold in the magnetic sector, but now with the sphaleronic perturbation added. The QNM ringdown to an intermediate attractor is no longer visible, only the QNM and tail to the final Schwarzschild black hole. A fit to the QNM yields $\lambda = -0.0819 \pm 0.2188i$ for w and $\lambda = -0.0801 \pm 0.2204i$ for ω. This is to be compared with the predicted QNM frequency in the magnetic sector [5] for the same mass (here $M = 1.139$), $\lambda = -0.0812 \pm 0.2180i$. Thus our results support the claim that the dominant Schwarzschild QNM frequency in the full EYM system is the same as in the magnetic sector. The fitted tail exponents are $p = -4.05$ for
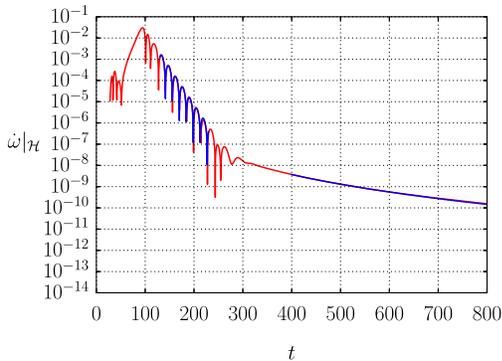
FIG. 15.   Time derivative of ω at the horizon (after it forms) as a function of time for $\tilde{A}_b = 10^{-2}$ and the same value for A_b as in the magnetic sector evolution (Fig. 13). The blue curves indicate the fits to the QNM and tail.

w and $p = -3.66$ for ω, both consistent with the exponent $p = -4$ observed in the magnetic sector.

V. CONCLUSIONS

This paper studies critical collapse in the general spherically symmetric Einstein-Yang-Mills (EYM) system. Compared to the magnetic ansatz most often used in numerical work so far, this has an additional physical degree of freedom, the "sphaleronic sector." Our main results can be summarized as follows.

In the magnetic sector, we confirm the phenomenology reported in [1]: both type I and type II critical collapse appear, depending on the family of initial data chosen. In addition to previous results, we find periodic wiggles in the type II scaling of the Ricci curvature invariant in subcritical evolutions that we relate to the echoing exponent. In type I collapse, our dynamical numerical evolutions show an approach to the static critical solution, the Bartnik-McKinnon soliton X_1, via a quasinormal mode (QNM) and a tail. We compare this with a calculation of the QNM of X_1 in linear perturbation theory. This is one of the few examples where a QNM ringdown to a nontrivial unstable static solution has been studied (other examples being the YM evolutions on a fixed Schwarzschild background in [5] and on the extremal Reissner-Nordström black hole in [23]). The presence of the QNM also causes damped oscillations of the apparent horizon mass as a function of the critical parameter distance in type I collapse (Fig. 5).

When the sphaleronic sector is turned on in the initial data, the picture of critical collapse changes completely. The type I behaviour now disappears and the generic critical behavior is type II. This is not surprising as the magnetic critical solution X_1 has an additional unstable mode in the sphaleronic sector [7]. The supercritical mass and subcritical curvature scaling exponents are very close to but, depending on the initial data, not identical with the ones found in the magnetic sector. We present a detailed comparison of the critical solution in the extended system with the critical solution in the magnetic ansatz. Looking at gauge invariant quantities I_1 and I_2 [see (A13) and (A14) for their definition] indicates that the two critical solutions are probably not identical. This follows from the observation that I_2 is nonzero (comparable in size to I_1) for critical evolutions of type II in the general ansatz, whereas it vanishes identically in the purely magnetic sector. We also find tentative evidence that exact discrete self-similarity as well as universality of the critical solution (with regard to different families of initial data) might be lost in the extended system. It could be that we are not yet sufficiently close to the critical point to see the true features of the critical solution. However, to push the bisection search further, we would have to use higher than the native double precision and in addition increase the numerical resolution much further, which did not seem feasible currently.

When a sphaleronic perturbation is added to initial data that would be type I critical in the magnetic sector, the type II polynomial scaling sets off at a finite distance from the critical point depending on the strength of the sphaleronic perturbation (Fig. 9). In such evolutions the magnetic type I critical solution X_1 can be seen as an intermediate attractor before the type II attractor is approached. We observe a QNM ringdown to this intermediate attractor, and again we find good agreement of the QNM frequency with a calculation in linear perturbation theory.

There is a third type of critical collapse in the magnetic sector of the EYM system discovered in [2] (and recently studied in more detail in [6]). Here evolutions on both sides of the threshold eventually settle down to Schwarzschild black holes but the YM potential is in different vacuum states. The critical solution is the colored black hole Y_1. Our simulations give tentative evidence of a QNM ringdown to the critical solution Y_1 but the time range during which this becomes visible is too short to be able to fit the QNM frequency. Higher precision would be required to uncover the QNM ringdown as well as possibly a polynomial tail around this intermediate unstable attractor. An independent confirmation of the existence of QNMs of colored black holes and their spectra will require a detailed analysis (boundary conditions) of the linearized problem.

When a sphaleronic perturbation is included in the initial data, the discontinuous transition of the YM potential w and the final black hole mass across the critical threshold is replaced with continuous ones. Thus we can no longer tune the initial data between two distinct outcomes, and the type III critical phenomenon disappears. This can be explained by the existence of an additional unstable mode of the Y_1 critical solution in the sphaleronic sector [15].

APPENDIX A: FIELD EQUATIONS

In this appendix we present the formulations of the field equations used in our two independent codes. The code used to study type I and type II collapse combines polar-areal coordinates (4) with the parametrization (1) of the YM connection. The code used to study type III collapse employs CMC-isotropic coordinates (5) and the parametrization (2) of

the YM connection. The choice of different parametrizations is insignificant and is only for "historical reasons" in the development of our codes. The EYM equations for a general spherically symmetric metric were also derived in the appendix of [2] and are consistent with our formulations. We use units in which $4\pi G g^{-2} = 1$, where G is Newton's constant and g is the YM coupling constant. Throughout an overdot denotes a time derivative and a dash a radial derivative.

1. Polar-areal coordinates

We introduce auxiliary variables Π, P and Y defined below by (A1), (A2) and (A5) and write the YM equations in first-order form (in time):

$$\dot{w} = Ae^{-\delta}\Pi + u\omega, \tag{A1}$$

$$\dot{\omega} = Ae^{-\delta}P - uw, \tag{A2}$$

$$\dot{\Pi} = (Ae^{-\delta}w')' + uP + w\frac{1 - w^2 - \omega^2}{r^2}e^{-\delta}, \tag{A3}$$

$$\dot{P} = (Ae^{-\delta}\omega')' - u\Pi + \omega\frac{1 - w^2 - \omega^2}{r^2}e^{-\delta}, \tag{A4}$$

$$\frac{r^2}{2}u' = -Ye^{-\delta}, \tag{A5}$$

$$Y' = \omega\Pi - wP. \tag{A6}$$

The Einstein equations and polar slicing condition reduce to

$$\dot{A} = 2re^{-\delta}A^{3/2}J_r, \tag{A7}$$

$$A' = \frac{1 - A}{r} - 2r\rho, \tag{A8}$$

$$\delta' = -\frac{r}{A}(\rho + S_r^r), \tag{A9}$$

where the components of the energy-momentum tensor are

$$\rho = \frac{Y^2}{r^4} + \frac{(1 - w^2 - \omega^2)^2}{4r^4} + \frac{A}{2r^2}(P^2 + \Pi^2 + w'^2 + \omega'^2), \tag{A10}$$

$$J_r = -\frac{\sqrt{A}}{r^2}(\Pi w' + P\omega'), \tag{A11}$$

$$\rho + S_r^r = \frac{A}{r^2}(P^2 + \Pi^2 + w'^2 + \omega'^2). \tag{A12}$$

We fix residual gauge freedom taking coordinated t to be proper time of central observer, i.e. we set $\delta(t, r = 0) = 0$.

In the analysis of type II critical collapse we plot the two gauge invariants

$$I_1 = -\frac{1}{8}\mathcal{F}^{(a)}_{\mu\nu}\mathcal{F}^{(a)\mu\nu}$$
$$= \frac{Y^2}{r^4} - \frac{(1-w^2-\omega^2)^2}{4r^4} + A\frac{\Pi^2 + P^2 - w'^2 - \omega'^2}{2r^2},$$
(A13)

$$I_2 = \frac{1}{8}\mathcal{F}^{(a)}_{\mu\nu}(*\mathcal{F}^{(a)\mu\nu})$$
$$= 2Y\frac{1-w^2-\omega^2}{r^4} + 2A\frac{Pw' - \Pi\omega'}{r^2},$$
(A14)

where the YM field strength tensor is

$$\mathcal{F}^{(a)}_{\mu\nu} = \nabla_\mu\mathcal{A}^{(a)}_\nu - \nabla_\nu\mathcal{A}^{(a)}_\mu + \varepsilon^{abc}\mathcal{A}^{(b)}_\mu\mathcal{A}^{(c)}_\nu$$
(A15)

and its Hodge dual is

$$*\mathcal{F}^{(a)}_{\mu\nu} = \sqrt{-g}\varepsilon_{\mu\nu\alpha\beta}\mathcal{F}^{(a)\alpha\beta}.$$
(A16)

The invariant I_1 is the Lagrangian of the YM field. The invariant I_2 has the interesting property that it vanishes in the magnetic sector.

2. CMC-isotropic coordinates

Following [8], we introduce auxiliary variables D_F, D_H and D_L defined below by (A17), (A18) and (A21) and write the YM equations in first-order form (in time).

$$\dot{F} = rXF' - \tilde{N}D_F + 2XF - r^2GH,$$
(A17)

$$\dot{H} = rXH' - \tilde{N}D_H + r^{-1}G' + GF + 3XH,$$
(A18)

$$\dot{D}_F = (rXD_F - \tilde{N}F')' + 2XD_F - 4\tilde{N}r^{-1}F'$$
$$- 2r^{-1}\tilde{N}' + G(D_L - r^2D_H)$$
$$+ \tilde{N}(-3F^2 - r^2H^2 + r^2F^3 + r^4FH^2),$$
(A19)

$$\dot{D}_H = (rXD_H - \tilde{N}H')' - r^{-1}(XD_L)'$$
$$- 3r^{-1}\tilde{N}'H + D_F(G - 2Xr^2H)$$
$$+ XD_H(1 + 2r^2F) - 2XFD_L$$
$$+ \tilde{N}(-4r^{-1}H + 2HrF' - 2FrH')$$
$$+ \tilde{N}(-4FH + r^2F^2H + r^4H^3),$$
(A20)

$$0 = -\tilde{N}D_L + rG' + G,$$
(A21)

$$0 = r^{-1}D_L' + 2F(D_L - r^2D_H) + 2D_H$$
$$+ 2r^2HD_F.$$
(A22)

We solve the following Einstein equations and coordinate conditions:

$$0 = -4\Omega\Omega'' + 6\Omega'^2 - 8\Omega r^{-1}\Omega' + \frac{3}{2}\Omega^2 r^4\pi^2$$
$$- \frac{2}{3}K^2 + 2\kappa\Omega^4\tilde{\rho},$$
(A23)

$$0 = \Omega(r\pi' + 5\pi) - 2r\Omega'\pi + \kappa\Omega^3 r^{-1}\tilde{J}^r,$$
(A24)

$$0 = -\Omega^2\tilde{N}'' + 3\Omega\Omega'\tilde{N}' - 2\Omega^2 r^{-1}\tilde{N}'$$
$$- \frac{3}{2}\Omega'^2\tilde{N} + \frac{1}{6}\tilde{N}K^2 + \frac{15}{8}\tilde{N}\Omega^2 r^4\pi^2$$
$$+ \frac{1}{2}\kappa\tilde{N}\Omega^4(\tilde{S} + 2\tilde{\rho}),$$
(A25)

$$X' = -\frac{3}{2}r\tilde{N}\pi.$$
(A26)

Here π denotes the only independent component of the traceless part of the ADM momentum in spherical symmetry [8]. The components $\tilde{\rho}$, $\tilde{S}$ and $\tilde{J}^r$ of the (conformally rescaled) energy-momentum tensor are given by

$$\tilde{\rho} = \tilde{S} = \frac{1}{2}[3D_L^2 - 2r^2(2D_LD_H - D_F^2 - r^2D_H^2)$$
$$+ 3B_L^2 - 2r^2(2B_LB_H - B_F^2 - r^2B_H^2)],$$
(A27)

$$r^{-1}\tilde{J}^r = 2[D_LB_F - D_FB_L + r^2(D_FB_H - D_HB_F)],$$
(A28)

where we have defined the magnetic field components

$$B_F = -3H - rH',$$
(A29)

$$B_H = r^{-1}F' + r^2H^2 + F^2,$$
(A30)

$$B_L = -2F + r^4H^2 + r^2F^2.$$
(A31)

APPENDIX B: LINEAR PERTURBATIONS OF STATIC SOLUTIONS

In this section we write down the equations governing linear perturbations of static EYM solutions explicitly and describe the procedures used to solve the linearized system of equations. We focus on static solutions with a regular center, and as argued in [16,17] we assume that the static solutions are purely magnetic.

Assuming time independence, i.e. $w(t, r) = w_s(r)$, $\delta(t, r) = \delta_s(r)$, $A(t, r) = A_s(r)$, and the magnetic ansatz, i.e. $\omega = Y = u = 0$, Eqs. (A1)–(A4) reduce to

$$w_s'' = \left(\frac{(w_s^2-1)^2}{2r^3A_s} + \frac{1-\frac{1}{A_s}}{r}\right)w_s' + \frac{w_s(w_s^2-1)}{r^2A_s}, \quad \text{(B1)}$$

$$\delta_s' = -\frac{w_s'^2}{r}, \quad \text{(B2)}$$

$$A_s' = \frac{1-A_s(w_s'^2+1)}{r} - \frac{(w_s^2-1)^2}{2r^3}. \quad \text{(B3)}$$

Regular solutions to (B1)–(B3) are the Bartnik-McKinnon solitons X_n [12]. For the purpose of the following analysis it is important to note the asymptotic $r \to \infty$ expansion of the static solutions, which reads

$$w_s(r) = \pm 1 + \frac{v_1}{r} + \mathcal{O}(r^{-2}), \quad \text{(B4)}$$

$$A_s(r) = 1 + \frac{a_1}{r} + \mathcal{O}(r^{-4}), \quad \text{(B5)}$$

$$\delta_s(r) = \delta_0 + \mathcal{O}(r^{-4}), \quad \text{(B6)}$$

where the higher order terms are uniquely determined by the v_1, a_1, and δ_0.

Next, with a perturbative ansatz of the form ($|\varepsilon| \ll 1$)

$$w(t,r) = w_s(r) + \varepsilon w_p(t,r), \quad \text{(B7)}$$

$$\omega(t,r) = \varepsilon\omega_p(t,r), \quad \text{(B8)}$$

$$u(t,r) = \varepsilon u_p(t,r), \quad \text{(B9)}$$

$$Y(t,r) = \varepsilon Y_p(t,r), \quad \text{(B10)}$$

$$A(t,r) = A_s(r)(1 + \varepsilon A_p(t,r)), \quad \text{(B11)}$$

$$\delta(t,r) = \delta_s(r) + \varepsilon\delta_p(t,r), \quad \text{(B12)}$$

we obtain the following set of linearized equations:

$$\frac{e^{2\delta_s}}{A_s}\ddot{w}_p = A_s w_p'' + \left(\frac{1-A_s}{r} - \frac{(w_s^2-1)^2}{2r^3}\right)w_p'$$
$$+ \left(\frac{1-3w_s^2}{r^2} - \frac{2w_s(w_s^2-1)w_s'}{r^3}\right)w_p$$
$$+ A_p\left(\frac{(w_s^2-1)^2w_s'}{2r^3} + \frac{w_s(w_s^2-1)}{r^2} - \frac{w_s'}{r}\right), \quad \text{(B13)}$$

$$\delta_p' = -\frac{2}{r}w_s'w_p, \quad \text{(B14)}$$

$$A_p' = -\frac{2w_s(w_s^2-1)w_p}{r^3A_s}$$
$$+ \left(\frac{(w_s^2-1)^2}{2r^2} - 1\right)\frac{A_p}{rA_s} - \frac{2}{r}w_s'w_p', \quad \text{(B15)}$$

$$\dot{A}_p = -\frac{2}{r}w_s'\dot{w}_p, \quad \text{(B16)}$$

$$\frac{e^{2\delta_s}}{A_s}\ddot{\omega}_p = A_s\omega_p'' + \left(\frac{1-A_s}{r} - \frac{(w_s^2-1)^2}{2r^3}\right)\omega_p'$$
$$- \frac{e^{2\delta_s}w_s\dot{u}_p}{A_s} + \frac{(1-w_s^2)\omega_p}{r^2}, \quad \text{(B17)}$$

$$\dot{Y}_p = A_s e^{-\delta_s}(w_s'\omega_p - w_s\omega_p'), \quad \text{(B18)}$$

$$Y_p' = -\frac{e^{\delta_s}w_s(w_s u_p + \dot{\omega}_p)}{A_s}, \quad \text{(B19)}$$

$$u_p' = -\frac{2}{r^2}e^{-\delta_s}Y_p. \quad \text{(B20)}$$

To simplify (B13)–(B20) we used the Eqs. (B1)–(B3) satisfied by static solutions. This explicitly shows that the linear perturbation splits into two independent classes: magnetic sector (B13)–(B16) and sphaleronic sector (B17)–(B20). We analyze them individually below.

1. Magnetic perturbations

Separation of variables

$$w_p(t,r) = \phi(r)e^{i\sigma t}, \quad A_p(t,r) = \alpha(r)e^{i\sigma t}, \quad \delta_p(t,r) = \beta(r)e^{i\sigma t}$$
$$\text{(B21)}$$

reduces (B13)–(B16) to a system of ordinary differential equations

$$\frac{e^{2\delta_s}\sigma^2}{A_s^2}\phi = -\phi'' + \left(-(1-A_s) + \frac{(1-w_s^2)^2}{2r^2}\right)\frac{1}{rA_s}\phi'$$
$$+ \left(-\frac{4w_s(1-w_s^2)w_s'}{r} + \frac{(1-w_s^2)^2w_s'^2}{r^2}\right.$$
$$\left. + (-1 + 3w_s^2 - 2w_s'^2)\right)\frac{1}{r^2A_s}\phi, \quad \text{(B22)}$$

$$\alpha = -\frac{2}{r}\phi w_s', \quad \text{(B23)}$$

$$\beta' = -\frac{2}{r}w_s'\phi'. \quad \text{(B24)}$$

Note that (B22) does not contain any metric perturbations; therefore the solution to (B22) fully determines the perturbation (B21) through the relations (B23)–(B24).

a. Unstable modes

Using standard methods (either shooting or a pseudospectral method) we look for solutions of (B13)–(B16) imposing asymptotically flat boundary conditions at spatial infinity. We find the value of the exponent of the unstable

mode of X_1 to be $\lambda = i\sigma = 2.562\,799\,802\,146\,866$. We also find, in agreement with previous studies [7], n unstable modes of the solution X_n. (We do not explicitly give the values for $X_{n>1}$ as these have more than one unstable mode and thus do not play any role in the critical collapse evolutions we consider here.)

b. Quasinormal modes

To find QNM we use the same shooting method as when looking for unstable modes. However, we now impose an outgoing boundary condition at spatial infinity. Taking

$$\phi(r) = e^{-irc_\infty}\xi(r), \qquad c_\infty = e^{\delta_0}, \qquad (\text{B25})$$

where δ_0 is the asymptotic value of $\delta(r)$ [cf. (B6)] and changing the independent variable to $z = 1/r$ we transform Eq. (B22) to

$$\xi''(z) + P(z)\xi'(z) + Q(z)\xi(z) = 0. \qquad (\text{B26})$$

The coefficients in the above equation (determined by the static solution and σ) have the following asymptotic form as $z \to 0$:

$$P(z) = \frac{p_{-2}}{z^2} + \mathcal{O}(z^{-1}), \qquad Q(z) = \frac{q_{-3}}{z^3} + \mathcal{O}(z^{-2}), \qquad (\text{B27})$$

with the expansion coefficients depending on v_1, a_1, δ_0, and σ. Thus $z = 0$ is an irregular singular point of Eq. (B26). However, assuming

$$\xi(z) = z^k \sum_{i\geq 0} \xi_i z^i, \qquad (\text{B28})$$

the indicial equation gives $k = -q_{-3}/p_{-2} = -ie^{\delta_0}a_1\sigma$, and we uniquely determine the expansion coefficients ξ_i [which are given in terms of the asymptotic expansion (B4)–(B6)].

Having two asymptotic solutions, one at the origin and the other obtained from the above asymptotic analysis, we integrate the Eq. (B6) starting from the two boundary points. Gluing the solutions at an intermediate point gives a quantization condition for σ. With this procedure we find the least damped QNM of X_1, whose frequency is $\lambda = -1.402\,33 \pm 3.603\,51i$. Interestingly enough with this method we were also able to obtain higher overtones (with faster damping rates) but these were not independently confirmed by time evolution and so we omit their presentation here.

2. Sphaleronic perturbations

Separation of variables

$$\omega_p(t,r) = \psi(r)e^{i\sigma t}, \; Y_p(t,r) = y(r)e^{i\sigma t}, \; u_p(t,r) = v(r)e^{i\sigma t},$$
$$(\text{B29})$$

reduces (B13)–(B16) to

$$-\frac{e^{2\delta_s}\sigma^2}{A_s}\psi = A_s\psi'' + \left(\frac{1-A_s}{r} - \frac{(w_s^2-1)^2}{2r^3}\right)\psi'$$
$$-\frac{i\sigma v e^{2\delta_s}w_s}{A_s} + \frac{\psi(1-w_s^2)}{r^2}, \qquad (\text{B30})$$

$$y = \frac{iA_s e^{-\delta_s}(w_s\psi' - \psi w_s')}{\sigma}, \qquad (\text{B31})$$

$$v' = \frac{2iA_s e^{-2\delta_s}(\psi w_s' - w_s\psi')}{r^2\sigma}. \qquad (\text{B32})$$

a. Unstable modes

In this sector we also find (as for the magnetic ansatz) n unstable modes for X_n. For the fundamental solution X_1 we have $\lambda = i\sigma = 2.783\,101\,206\,773\,3285$.

b. Quasinormal modes

In the nonlinear evolution we see no sign of quasinormal modes within the sphaleronic sector. Thus we leave open the question of their existence.

APPENDIX C: NUMERICAL METHODS

In this section we briefly describe the numerical methods used in our two independent codes.

1. Type I and type II collapse

For the time evolution we use the method of lines with a second-order finite-difference discretization in space and the explicit Runge-Kutta time integration scheme DOPRI (a fifth-order adaptive method) [24]. To refine the central region of the spatial domain we use a nonequidistant grid. The spacing between grid points is fixed over time. We choose a logarithmic distribution which concentrates grid points close to $r = 0$ and has physical extent $r \in [0, r_m]$, explicitly

$$r_i = r_m \log\left(1 - \left(\frac{i}{N}\right)^k\right) / \log\left(1 - \left(\frac{N-1}{N}\right)^k\right), \qquad (\text{C1})$$

$i = 0, 1, \ldots N-1$. The two free parameters k and r_m in (C1) were chosen to reach a compromise between higher resolution close to the origin (sufficient to represent fine structures of solutions) and a sufficiently large physical extent of the grid (so that the numerical solution is not affected by the presence of a timelike boundary). At the outer boundary we use one-sided finite-difference stencils. Most of the simulations were carried out using $k = 3/2$ and $r_m = 200$ or $r_m = 400$. We typically take from $N = 1 + 2^{10}$ to $N = 1 + 2^{12}$ grid points.

2. Type III collapse

This code uses the method of lines with a fourth-order finite-difference discretization in space and the standard fourth-order Runge-Kutta method for the time evolution. Ordinary differential equations with respect to radius are solved using a Newton-Raphson method combined with a direct band-diagonal solver. In the first phase of the evolution, the radial grid is uniform and ranges from the origin to future null infinity, where one-sided finite differences are used. When a black hole forms, an excision boundary is placed just inside the apparent horizon, where again one-sided stencils are used. The YM variable G is fixed to zero at the excision boundary. In this second phase of the evolution, the radial grid is nonuniform in order to provide more resolution close to the horizon, where the fields have large gradients. Typical resolutions range from 500 (Figs. 11–13) to 4000 (Figs. 14 and 15) radial grid points. More details on the numerical implementation can be found in [6,8].

[1] M. W. Choptuik, T. Chmaj, and P. Bizoń, Phys. Rev. Lett. **77**, 424 (1996).

[2] M. W. Choptuik, E. Hirschmann, and R. Marsa, Phys. Rev. D **60**, 124011 (1999).

[3] A. Zenginoğlu, Classical Quantum Gravity **25**, 175013 (2008).

[4] M. Pürrer and P. C. Aichelburg, Classical Quantum Gravity **26**, 035004 (2009).

[5] P. Bizoń, A. Rostworowski, and A. Zenginoğlu, Classical Quantum Gravity **27**, 175003 (2010).

[6] O. Rinne, Phys. Rev. D **90**, 124084 (2014).

[7] G. Lavrelashvili and D. Maison, Phys. Lett. B **343**, 214 (1995).

[8] O. Rinne and V. Moncrief, Classical Quantum Gravity **30**, 095009 (2013).

[9] P. Bizoń, Acta Cosmol. **22**, 81 (1996).

[10] M. W. Choptuik, Prog. Theor. Phys. Suppl. **136**, 353 (1999).

[11] C. Gundlach and J. M. Martín-García, Living Rev. Relativity **10**, 5 (2007).

[12] R. Bartnik and J. McKinnon, Phys. Rev. Lett. **61**, 141 (1988).

[13] P. Bizoń, Phys. Rev. Lett. **64**, 2844 (1990).

[14] M. S. Volkov and D. V. Gal'tsov, Pis'ma Zh. Éksp. Teor. Fiz. **50**, 312 (1989), JETP Lett. **50**, 346 (1989).

[15] M. S. Volkov, O. Brodbeck, G. Lavrelashvili, and N. Straumann, Phys. Lett. B **349**, 438 (1995).

[16] D. V. Gal'tsov and A. A. Ershov, Phys. Lett. **138A**, 160 (1989).

[17] A. A. Ershov and D. V. Gal'tsov, Phys. Lett. **150A**, 159 (1990).

[18] E. Witten, Phys. Rev. Lett. **38**, 121 (1977).

[19] C. Gu and H. Hu, Commun. Math. Phys. **79**, 75 (1981).

[20] C. Gundlach, Phys. Rev. D **55**, 6002 (1997).

[21] S. Hod and T. Piran, Phys. Rev. D **55**, R440 (1997).

[22] P. Bizoń, T. Chmaj, and A. Rostworowski, Classical Quantum Gravity **24**, F55 (2007).

[23] P. Bizoń and M. Kahl, Classical Quantum Gravity **33**, 175013 (2016).

[24] E. Hairer, G. Wanner, and S. P. Nørsett, *Solving Ordinary Differential Equations I*, Springer Series in Computational Mathematics, Vol. 8 (Springer, Berlin, Heidelberg, 1993).